OPEN

Correspondence and requests for materials should be addressed to C.B. (christiane.becker@helmholtz-berlin.de)

5 × 5 cm² silicon photonic crystal slabs on glass and plastic foil exhibiting broadband absorption and high-intensity near-fields

C. Becker[1], P. Wyss[1], D. Eisenhauer[1], J. Probst[1], V. Preidel[1], M. Hammerschmidt[2] & S. Burger[2]

[1]Helmholtz-Zentrum Berlin für Materialien und Energie, Kekuléstr. 5, 12489 Berlin, Germany, [2]Zuse Institute Berlin, Takustraße 7, 14195 Berlin, Germany.

Crystalline silicon photonic crystal slabs are widely used in various photonics applications. So far, the commercial success of such structures is still limited owing to the lack of cost-effective fabrication processes enabling large nanopatterned areas ($\gg$ 1 cm²). We present a simple method for producing crystalline silicon nanohole arrays of up to 5 × 5 cm² size with lattice pitches between 600 and 1000 nm on glass and flexible plastic substrates. Exclusively up-scalable, fast fabrication processes are applied such as nanoimprint-lithography and silicon evaporation. The broadband light trapping efficiency of the arrays is among the best values reported for large-area experimental crystalline silicon nanostructures. Further, measured photonic crystal resonance modes are in good accordance with light scattering simulations predicting strong near-field intensity enhancements greater than 500. Hence, the large-area silicon nanohole arrays might become a promising platform for ultrathin solar cells on lightweight substrates, high-sensitive optical biosensors, and nonlinear optics.

C rystalline silicon slabs with a hexagonal lattice of nanoholes are among the most common photonic crystal structures. A hexagonal array of nanoholes in a high refractive index material such as silicon favors the formation of robust and large photonic band gaps[1]. Silicon nanohole arrays also theoretically represent an advantageous solar cell absorber geometry revealing broadband light trapping possibly even outperforming periodic arrays of cylindrical silicon nanowires[2]. For the fabrication of such silicon nanophotonic structures on submillimeter scale mature, industry-compatible techniques are existing in complementary metal-oxide–semiconductor and silicon-on-insulator (SOI) technology. The implementation of crystalline silicon photonic crystal slabs into large-scale applications ($\gg$ 1 cm²) such as photovoltaics or biosensors, however, requires alternative low-cost and up-scalable processes enabling much larger nanopatterned active areas. Furthermore, lightweight and flexible substrates would be preferable.

Here, we present a nanophotonic platform based on crystalline silicon nanohole arrays on areas up to 5 × 5 cm² on glass or plastic substrates. It combines the potentially high electronic material quality and the high refractive index *n* of a crystalline semiconducting material, with the advantages of organics and thin-film technologies - namely large-area fabrication techniques, the use of low cost, flexible, lightweight substrates and low material consumption. Nanoimprint-lithography (NIL) is applied for quick and uncomplicated nano-patterning of the substrate template requiring only limited machine processing time[3]. Resolution and structural diversity are only limited by the availability of suitable master structures. Therefore, NIL is a very popular technique applied for systematic nanostructuring of solar cell devices[4–6] and has also been applied for the fabrication of photonic crystals based on SOI[7] and chalcogenide glasses on plastic substrates[8]. The further processing steps – silicon evaporation, thermal annealing and wet-chemical etching – are also available on large areas.

The crystalline silicon nanostructures on glass or plastic substrate are investigated with regard to two representative fields of application, both requiring large active nanostructured areas. 1.) In photovoltaics strong efforts are undertaken to reduce costs by diminishing the volume of the active material using ultrathin films. Broadband absorption in such ultrathin solar cells is rendered possible by periodic nanostructuring on wavelength scale[2,9–13]. In 2010, it has been shown that such nanophotonic light trapping schemes even enable a light path enhancement

in the absorbing film beyond the ray optics limit of $4n^2$ [12,14]. In this study, the silicon nanohole arrays are regarded as model system in order to experimentally find design guide lines for optical broadband absorption in nanostructured ultrathin solar cells. 2.) Periodic nanostructures are also intensively investigated for biosensor applications making use of high-intensity near fields in the vicinity of the photonic crystal surface or at photonic crystal defects. There are two main detection modes in optical biosensing, both benefitting from the presence of a photonic crystal: Fluorescence measurements harvest the enhanced interaction between the evanescent electromagnetic fields and the analyte at the photonic crystal surface [15,16]. Label-free optical biosensing relies on the detection of the small refractive index change induced by bio-molecule interaction with photonic crystal interfaces [17]. E.g. Lee et al. have demonstrated an extremely sensitive biosensor measuring the small refractive index change induced by bio-molecule immobilization in the pores of a silicon nanohole slab [18]. In either case, the availability of large-area photonic crystals would strongly facilitate the optical biosensing process as a large sensing area allows for a large and well-collimated read-out beam. While in photovoltaics the silicon nanostructures have to be designed in such a way that light is concentrated and absorbed in the active crystalline silicon material, biosensor applications necessitate high-intensity near fields at the surface or in the nanoholes of the slab. Therefore, the nanophotonic structures have to be designed accordingly with respect to their specific application. Here, we choose crystalline silicon as photonic crystal material due to several reasons. On the one hand, crystalline Si is an attractive material for photovoltaic applications owing to its natural abundance enabling the production of solar cells on terawatt scale [19], its non-toxicity and environmental harmlessness, its nearly perfect band gap for single junction devices, and the great experience and knowledge about the material. On the other hand, silicon enables strong photonic crystal effects because of its large refractive index above 3.5.

Results

Fabrication. Starting point is a master nanostructure in a silicon wafer with the inverse of the anticipated nanohole configuration – hexagonally arrayed cylinders. Here, the masters were fabricated by either electron beam lithography technology (pitch size 600 to 800 nm) [20] or mask based UV lithography (pitch size 1000 nm). We designed three different fields of 6×8 mm² composed of hexagonal lattices and varying pitches p of 600, 700 and 800 nm with the corresponding cylinder diameters of 454, 530 and 622 nm, respectively, for the light trapping experiments and photonic crystal mode analysis. For the demonstration of up-scalability of the fabrication procedure we use a 5×5 cm² masterstructure with a hexagonal lattice of cylinders with 1000 nm pitch and 470 nm diameter.

The next step is the replication of the silicon master nanostructure directly onto a glass substrate by using the UV-nanoimprint lithography (UV-NIL) technology: First, a soft nanoimprint stamp is prepared as a mold for the replication process by pouring poly-(dimethyl) siloxane (PDMS) onto the master nanostructure and subsequent curing at 70°C. By imprinting the PDMS-stamp onto sol-gel coated glasses with subsequent UV-curing, the master nanostructure can be replicated multiple times. A final thermal annealing step causes a shrinkage of the sol-gel features of about 40-45% such that the original cylinder diameters of the masterstructures of 454, 530, 622, and 470 nm decrease to about 250, 310, 360, and 280 nm as measured by atomic force microscopy. The lattice pitch does not change. We use a custom-made hybride UV-curable sol-gel resist prepared with silicon alkoxides [21] as further processing requires high temperature stability up to 600°C. More details about the UV-NIL replication process can be found in the Methods section and in reference [22].

In the last fabrication step these high-temperature stable nanostructured sol-gel coated glass substrates are used as a template for the fabrication of the 2D large-area crystalline silicon nanohole arrays, as already shown for similar micrometer sized structures [23]. The process chain is schematically displayed in Fig. 1a: An amorphous silicon layer is deposited by electron-beam evaporation, a directional non-conformal deposition method [24], followed by a self-organized solid phase crystallization process by thermal annealing for several hours at 600°C (1). The crystallization of the silicon parts deposited on steep flanks of the underlying substrate is suppressed. These residual amorphous parts are selectively removed by wet-chemical etching (2). The solid phase crystallization process results in a polycrystalline silicon film. While bulk films typically exhibit grain sizes in the order of 1–3 μm [6], the crystal size of the nanostructured films investigated here seems to be restricted by the lattice pitch and is therefore slightly smaller (0.5–1 μm). Scanning electron microscopic images indicate that the physical dimensions of the films (e.g. thickness) don't change significantly during the crystallization process. The crystalline silicon nanohole arrays are finally produced by mechanical abrasion of the remaining silicon nanotips (3). Detaching of the Si features is achieved by rubbing the sample against a wet clean room wipe. A subsequent rinse with deionized water is applied to wash off any residual Si nanotips. If the silicon layer thickness is smaller than the height of the sol-gel features sol-gel nanotips are also removed. Due to the geometrical emission characteristic of the silicon evaporation process the resulting nanoholes exhibit a tapering angle of about 15°–18°. The transfer of the silicon structures to a lightweight plastic substrate is realized by adhering adhesive tape to the silicon surface (4) and dissolving the glass and sol-gel in concentrated hydrofluoric acid (5).

It is noted that the solid phase crystallization approach described here is not the only method for the fabrication of large-area silicon nanostructures on nanoimprinted glasses. The nanopatterned temperature-stable glass substrates could also serve as template for other silicon thin-film technologies, e.g. for liquid phase crystallized silicon thin-film material recently demonstrating wafer quality electronic properties and therefore being an excellent candidate for solar cell applications [25]. However, here we exclude electronic material quality considerations and concentrate on experimental and computational investigations of the optical performance of large-area silicon nanohole arrays.

The resulting silicon nanostructures with 1000 nm pitch are shown in Fig. 1b–g in three different magnifications, images taken by camera, optical microscope and scanning electron microscope. The silicon photonic crystal slabs on glass substrate exhibit only a very low density of lattice imperfections and other defects. The silicon nanohole arrays on plastic exhibit cracks in about millimeter distance. This might be explained by a certain tension in the silicon layer on glass relaxing when the glass is removed by hydrofluoric acid. The opening angle of the tapered nanoholes can be estimated by comparing Fig. 1e (view direction from top) and Fig. 1g (view direction from the former glass-silicon interface side). With an upper hole diameter of about 500 nm and a lower diameter of around 300 nm the hole tapering angle can be determined to about 15°. When the silicon layer thickness (375 nm) is larger than the height of the sol-gel nanotips (240 nm) the nanotips are not removed in the mechanical abrasion step and can still be seen inside the nanoholes on the glass substrate (Fig. 1e). However, they are removed during the etching process with hydrofluoric acid in case of the structures on plastic foil (Fig. 1g).

Figure 2 depicts the surface of a crystalline silicon nanohole array with 600 nm lattice pitch, hole central diameter 385 nm and hole sidewall angle 17°. Here, the sol-gel nanotips were high enough such that they could be removed together with the silicon tips during the mechanical abrasion process (Fig. 1a (3)). The two high-symmetry directions of the hexagonal lattice, Γ-K and Γ-M, are indicated by
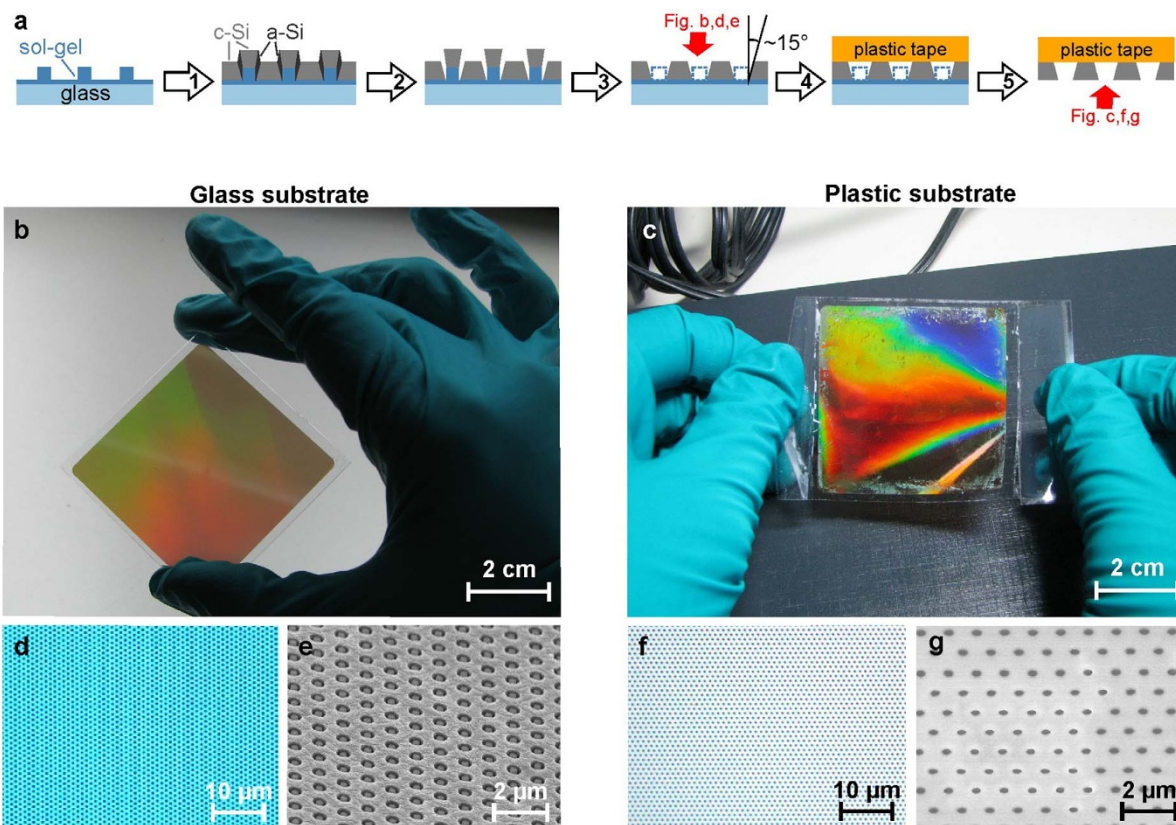
Figure 1 | Large-area crystalline silicon nanohole arrays on nanoimprinted sol-gel coated glass and on flexible plastic foil. (a) Fabrication process chain: 1) Physical evaporation of amorphous silicon on nanopatterned substrates and subsequent self-organized solid phase crystallization by thermal annealing; 2) Removal of amorphous silicon parts by wet-chemical etching; 3) Removal of silicon tips and optional removal of sol-gel cylinders by mechanical abrasion; 4) Attachment of adhesive tape; 5) Removal of glass and sol-gel by concentrated hydrofluoric acid. Small red arrows indicate the view direction of images. (b)–(g) 5×5 cm² large hexagonal crystalline silicon truncated nanohole arrays with 1000 nm period, 375 nm layer thickness and about 500 nm and 300 nm upper and lower hole diameter, on nanoimprinted sol-gel-coated glass substrate (b,d,e) and transferred to flexible plastic foil (c,f,g) imaged in three different magnifications by camera (b,c), optical microscope (d,f) and scanning electron microscope (e,g, view 30° tilted).

arrows. These structures are investigated with regard to their light trapping and near-field energy enhancement properties. Although the area of this prototype sample was 6×8 mm² only, there are no principal limitations in terms of up-scalability to larger areas up to 5×5 cm².

Light trapping properties. Figure 3 summarizes the absorption properties of crystalline silicon nanohole arrays in hexagonal geometry with 600, 700 and 800 nm pitch and planar reference films
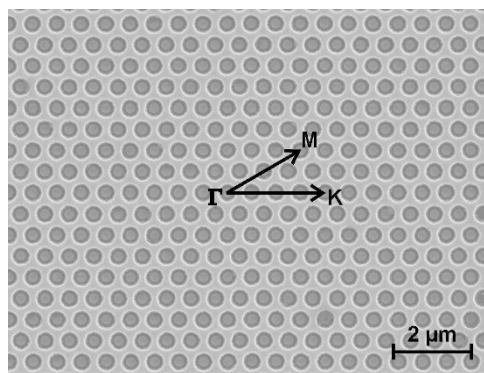

Figure 2 | Scanning electron microscope image of a crystalline silicon nanohole array on nanoimprinted sol-gel coated glass with a lattice pitch of 600 nm. The high-symmetry directions of the hexagonal lattice, Γ-K and Γ-M, are marked by arrows.

with the same a layer thickness of $d = 390$ nm. A hole central diameter around 0.64 times the pitch was chosen corresponding to a fill fraction of 63% as depicted in Fig. 3a. The absorption spectra shown in Fig. 3b were measured inside an integrating sphere with the surface normal slightly tilted by 10 degrees in Γ-K direction with respect to the incident light. The benchmarking Yablonovitch limit assuming perfect antireflection and light trapping, calculated by $A_{Yablonovitch} = 1 - 1/(1 + 4n^2\alpha d)$ [26,27] with α the absorption coefficient and n the refractive index of crystalline silicon, is represented by a thick red line. Although the silicon nanohole arrays only consist of about 63% of the silicon volume of a planar film of the same thickness, the absorption is considerably increased for wavelengths larger than about 450 nm (thin lines). A lattice period of 600 nm yields the largest integrated absorption which is in accordance with recent numerical studies indicating that a period from 500 to 600 nm enables the best light trapping properties of ultrathin crystalline silicon nanohole arrays [2,28]. In order to evaluate the entire potential of such ultrathin absorbers we covered the 600 nm periodic array with an antireflective coating (ARC) consisting of a 85 nm silicon nitride film, and coated the rear side of the glass substrate with a white paint back reflector (BR). The respective absorption curve is shown as thick blue line. The antireflective effect at shorter wavelengths is clearly visible, but also the amplified light trapping in the near infrared region is obvious. The increased absorption is even stable for larger angles of incidence up to 60 degrees (Fig. 3c) which is of great importance for a high solar cell performance at different positions of the sun varying during the day and the year. No remarkable difference of absorption is visible
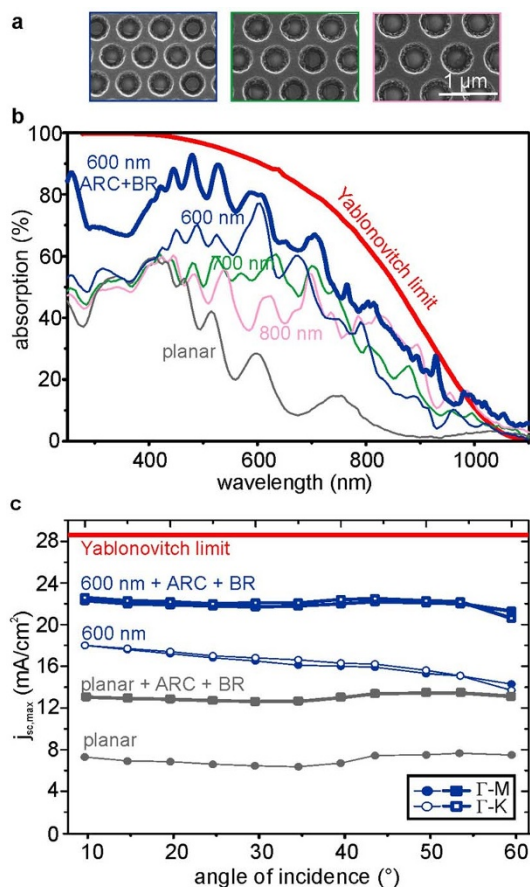
Figure 3 | Absorption properties of hexagonal crystalline silicon nanohole arrays on glass with 390 nm layer thickness. (a) SEM images depicting samples with pitch $p = 600$ nm, 700 nm, 800 nm (from left to right). (b) Absorption for different lattice periods without (thin lines) and with (thick line) 85 nm SiN antireflective coating (ARC) and white paint back reflector (BR). For practical reasons light impinges at 10° from normal incidence in Γ-K direction during measurements. The red curve represents the Yablonovitch limit assuming perfect antireflection and light trapping. (c) Maximum short circuit current density $j_{sc,max}$ achievable in ultrathin c-Si solar cells with 600 nm hexagonal nanohole array absorber geometry (blue) and respective planar films (grey) without (thin lines) and with ARC and BR (thick lines). $j_{sc,max}$ has been calculated considering the global solar spectrum AM1.5g.

when comparing the measurements with the samples tilted over the two different high-symmetry directions of the hexagonal lattice Γ-M and Γ-K. Hence, the hexagonal lattice geometry seems to be sufficiently isotropic for light trapping at diffuse irradiation conditions. All absorption measurements are summarized in Fig. 3c indicating the maximum short circuit current density $j_{sc,max}$ achievable with 390 nm thin crystalline silicon absorbers of different geometries using the solar irradiance spectrum AM1.5g in the spectral range from 300 to 1100 nm [29]. While planar films without any further treatment exhibit a $j_{sc,max}$ of only around 7 mA/cm², $j_{sc,max}$ increases to around 18 mA/cm² for 600 nm periodic nanohole arrays. By addition of afore mentioned ARC and BR components values about 13.2 mA/cm² and 22.6 mA/cm² are achieved for planar and 600 nm periodic films, respectively.

In order to assess the light trapping performance of the crystalline silicon nanohole arrays and to compare it with other silicon nanostructures for solar cells from the literature, we calculated the light trapping efficiency LTE inspired by a recent study by Schuster et al.[30]. This figure of merit is given by $LTE = (j_{sc,max} - j_{sc,plan})/(j_{sc,Yabl} - j_{sc,double\ pass})$ with $j_{sc,max}$ the maximum achievable short circuit

current density of the nanostructure to be evaluated, $j_{sc,plan}$ the respective value for a planar reference system with same ARC and BR, $j_{sc,Yabl}$ the short circuit current density assuming perfect antireflection and light trapping (28.6 mA/cm² for $d = 390$ nm) and $j_{sc,double\ pass}$ determined by $A_{double\ pass} = 1 - \exp(-2\alpha d)$ assuming a planar film with perfect antireflection and a perfect back reflector (10.6 mA/cm² for $d = 390$ nm), and calculated an LTE of 0.52. As a small parasitic absorption contribution is expected at wavelengths below 350 nm by the glass and the sol-gel layer, and at wavelengths above 1000 nm by the white paint back reflector, we also calculated LTE considering the absorption in the range from 350 to 1000 nm only. The result is the same ($LTE_{350-1000} = 0.52$) as the difference $(j_{sc,max} - j_{sc,plan})_{350-1000}$ hardly changes in this case. The LTE values presented here are larger than the highest values of experimentally realized nanostructured crystalline silicon thin-film solar cells (LTE ≤ 0.3) given in the literature survey of reference[30], but smaller than the LTE yielded by theoretical studies. The work by Han and Chen[2] for instance, describing silicon nanohole structures which are very similar to the geometries shown here in this study, yields an LTE value of 0.92 underlining the high potential of a nanohole geometry. The future vision is to prepare nanohole structures in a crystalline silicon thin-film material featuring a competitive electronic material quality, e.g. prepared by liquid phase crystallization[25] or layer transfer[31], in order to realize highly efficient photovoltaic devices.

Near field energy enhancement. For light trapping in the crystalline silicon nanohole arrays the absorption properties in the wavelength regime below the (indirect) electronic band gap of silicon, i.e. $\lambda < 1100$ nm, were of particular interest. In contrast, in order to enlarge the electric field energy close to the photonic crystal surface the presence of absorption would be rather counterproductive. Therefore, in this section we concentrate on wavelengths with no or only little absorption at wavelengths $\lambda > 850$ nm.

We have performed angular resolved reflection measurements of light incident on the sample with $p = 600$ nm, central diameter 385 nm and sidewall angle 17°. The geometry parameters have been obtained using SEM. We have used light of S and P polarizations incident in tilted Γ-K direction and Γ-M direction, and we investigated a wavelength range of 850 nm to 1800 nm and an angular range of 10 to 80 degrees. The resulting spectra are displayed in Fig. 4 (left column). Several distinct resonances with strong dependence on wavelength and incidence angle are clearly visible for both polarizations and directions of incidence. These features obviously correspond to resonance modes which are excited in the photonic crystal. Angular resolved spectroscopy is a well-known method for determination of the properties of photonic crystal band structures[32]. For a quantitative understanding we have performed simulations of the experimental setup using the methods described above. We find a very good agreement between experimental and simulation results which are displayed in Fig. 4 (center column). The slight red-shift of the computed spectra compared to the experimental measurements can be explained by a small deviation between the simulated geometry and the real structures. Further the linewidths of the resonances in the measured spectra are broader than in the simulated spectra. We attribute the broadening to the finite spectral and angular resolution of the source in the experiments, and possibly also to experimental structures deviations from ideal periodicity.

From the simulations we also extract information on the obtained field energy enhancement by integrating the electromagnetic field energy density inside the pores and in a 100 nm-thin layer above the pores and by normalizing the field energy to the energy of a plane wave in the same volume in free space. The dependence of field energy enhancement on wavelength and angle of incidence of the corresponding plane waves is displayed in Fig. 4 (right column). Sharp features of strong enhancement are observed in these spectra. As can be expected, these features are aligned with the photonic
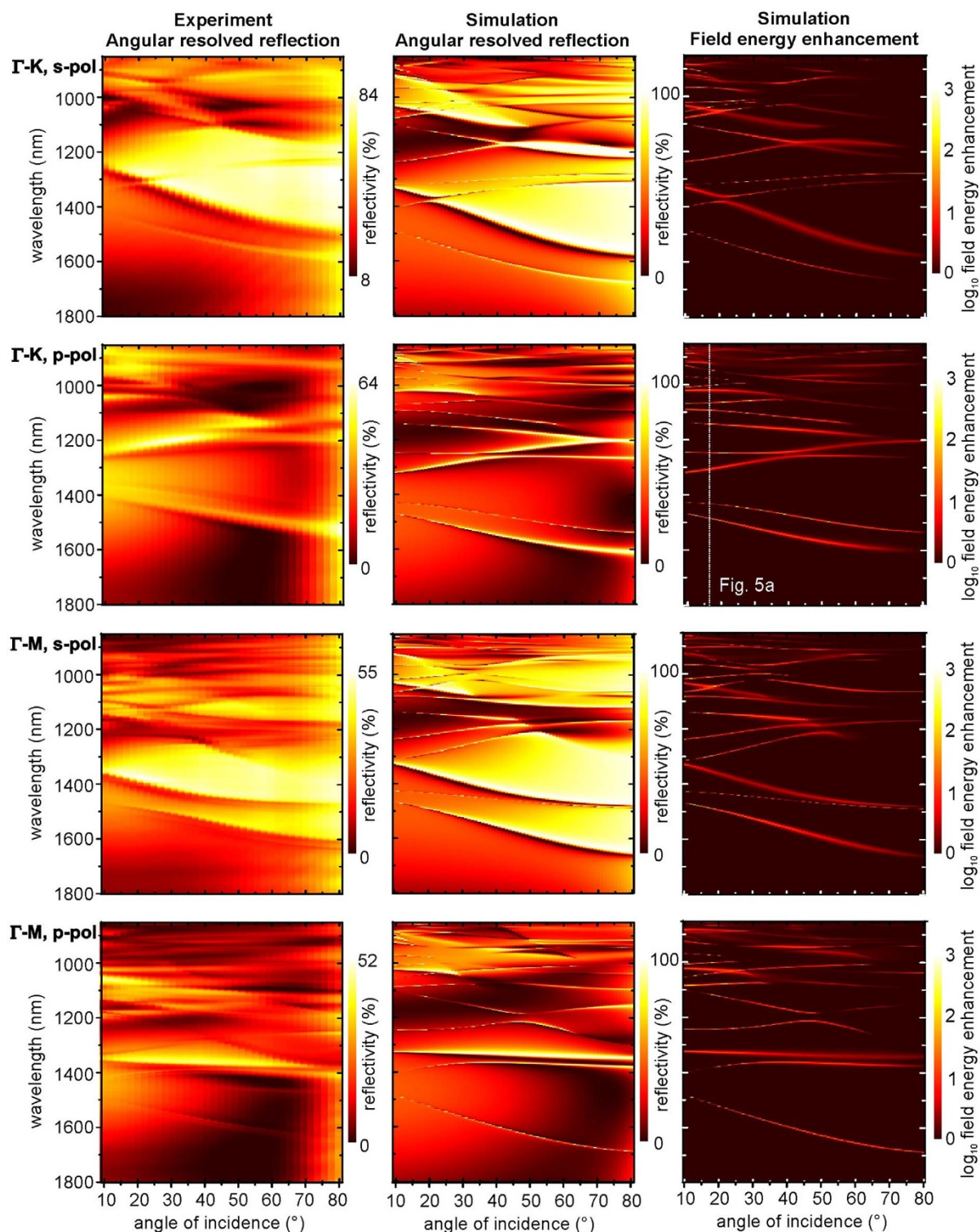
4

Figure 4 | Leaky modes of a hexagonal 600 nm periodic crystalline silicon nanohole array coupling to the incident light. Angular resolved reflection for Γ-K and Γ-M direction and both incident polarizations, experimental results (left column) and simulation results (center column). Respective simulated field energy enhancement at photonic crystal surface (hole and 100 nm air layer above) normalized by the respective field energy of a plane wave in the same volume in air (right column). The dashed line indicates the spectrum shown in Fig. 5a.

crystal resonances as detected in the reflection spectra. Strongest observed near field enhancement for the investigated structure is a factor of about 550 (Γ-K, P Pol, incident angle 17°, λ = 1006 nm). Due to imperfections of the fabricated structure the experimental enhancement may be smaller or even larger, however, given the very good agreement of the reflection spectra we expect simulated and

experimentally realized enhancement also to be at least in qualitative agreement.

Figure 5a shows a single simulated enhancement spectrum for a distinct angle of incidence (Γ-K, p-polarized, incident angle 17°) taken from the results visualized also in Fig. 4. Three distinct wavelengths are marked with arrows. At these wavelengths we have
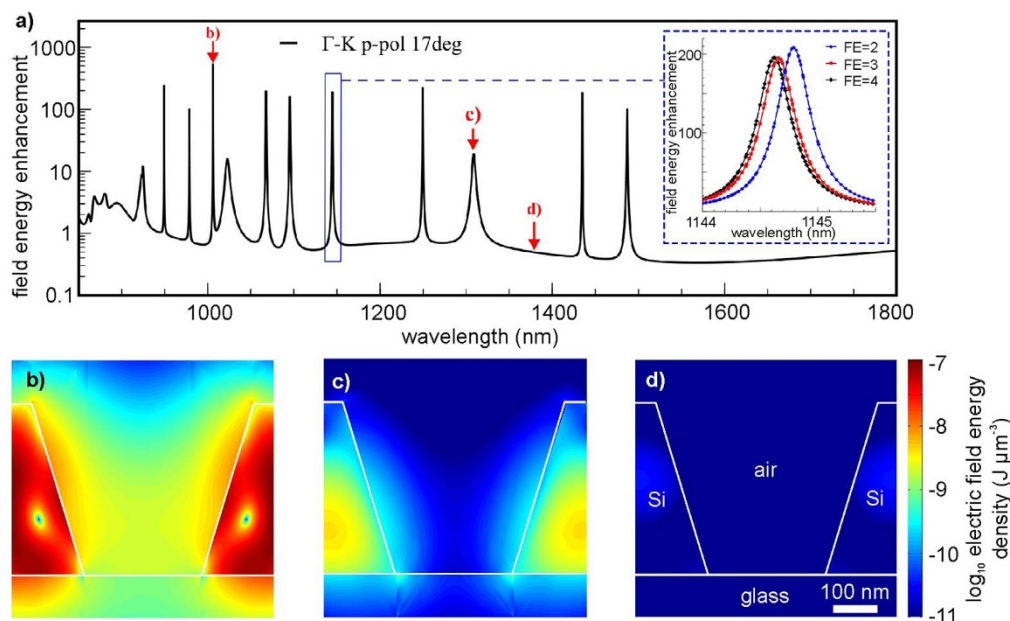
Figure 5 | (a) Simulated electric field energy enhancement for 17° angle of incidence in Γ-K direction for p-polarized light, i.e. the electric field vector parallel to the plane of incidence. (b–d) Simulated intensity distributions of tapered nanohole arrays in crystalline silicon (cut through the middle of the air hole perpendicular to the plane of incidence) for λ = 1006 nm (b, field energy enhancement in air region 550), λ = 1309 nm (c, field energy enhancement 14) and λ = 1379 nm (field energy enhancement < 1).

exported and visualized the electric field energy density in 2D cross sections through a pore of the photonic crystal. These near field distributions are visualized in Fig. 5b–d. It can clearly be seen that the sharp peaks in the enhancement spectra correspond to cases where Bloch modes in the photonic crystal are excited. Due to the resonant excitation of these modes, very high field intensities are reached, especially also inside the material. However, the field leaking into the pores still is orders of magnitude larger than in the case where no resonances are excited (Fig. 5d). The inset in Fig. 5a shows a specific resonance, computed at different numerical resolution (FE = 2: second order finite-elements, FE = 3: third-order finite-elements, FE = 4: fourth order finite elements). The very good convergence with finite-element degree allows concluding that numerical errors of the investigated physical quantities well below one percent can easily be reached throughout the full parameter range of interest. This ensures that deviations between experiment and simulation can be attributed to geometrical or material model deviations, but not to insufficient numerical resolution.

The field energy enhancements up to 550 shown here rely on an undisturbed photonic crystal. The implementation of a point-like or extended defect locally disturbing the periodic structure can lead to a formation of a defect mode within the bandgap with high quality factor and hence even stronger intensity enhancement.

Discussion and conclusion

Crystalline silicon nanohole arrays with hexagonal lattice pitches between 600 and 1000 nm have been prepared on nanoimprinted glasses and flexible plastic substrates on areas up to 5 × 5 cm². The exclusive application of low-cost and up-scalable processes such as nanoimprint-lithography, physical evaporation of silicon, thermal annealing and wet-chemical etching opens up the possibility of direct implementation on industry-scale production. The structures have been investigated with a view to ultrathin photovoltaics and biosensing, representing two fields of application requiring large nanopatterned areas. The crystalline silicon nanohole arrays demonstrated strong broadband absorption properties being among the best light trapping efficiencies reported for large-area experimental crystalline silicon nanostructures. Angular resolved reflection measurements

revealed distinct resonances that were assigned to leaky photonic crystal eigenmodes and were in excellent agreement with respective finite element simulations. The field energy in the pores and in the area 100 nm above the photonic crystal surface was computed and yielded enhancement factors with respect to a plane wave in an equivalent free space volume greater than 500. The range of applications of the large-area silicon nanohole arrays on glass and plastic foil presented here is not only restricted to photovoltaic or biosensor applications, but also inspires to be a platform for nonlinear optics, spectral conversion and light-emitting diodes.

Methods

Nanoimprint-lithography. Once a masterstructure is prepared, a preliminary surface silanization is done in a desiccator connected to a vacuum line avoiding possible adhesions between the polymer mold and the silicon master during the later molding procedure. The prepared silicon master is placed in a petri dish together with a small watch glass containing a few drops of tridecafluoro-1,1,2,2-tetrahydrooctyle-1-trichlorosilane (TFOCS). Then by turning on the vacuum the TFOCS vaporized in the chamber forms a monolayer of anti-sticking agent onto the silicon master surface. After the functionalization the polymer mold can be prepared by mixing the poly-(dimethyl) siloxane and its catalyst (PDMS, Elastosil RT A/B 601 from Wacker) with a ratio of 9 : 1 inside a clean PTFE-beaker corresponding to 18 grams of the silicone base A mixed with 2 grams of catalyst B in our experiment. The PDMS is thoroughly mixed during 5 minutes with a cleaned glass stick and degassed during 10 minutes in a desiccator connected to the vacuum system. Then the PDMS is poured directly onto the silanized master and subsequently cured in an oven at 70°C during 30 minutes. The so called PDMS soft-stamp can then be gently peeled off from the master and used as a mold for the replication process.

The sol-gel is applied with the desired thickness onto some pre-cleaned glass substrate (SCHOTT AF 37 or Corning Eagle) by dipcoating. The PDMS stamp is then directly applied onto the sol-gel resist and cured with a 400 nm UV lamp for about 4 minutes. After UV-curing, the stamp is again carefully peeled off from the glass substrate revealing the imprinted nanopillar arrays. Finally the nanostructures are thermally annealed at about 600°C during 1 hour in order to remove the remaining organics and increase the silica densification. This annealing step leads to shrinkage of the dimensions of the original nanofeatures (cylinder height and diameter) about 40–45% while the lattice pitch remains unaffected.

Computation. Optical properties of nanohole arrays are computed using simulations based on a finite-element method (FEM). For this, geometrical values of the nanohole array (pitch p, layer thickness d, hole central diameter, sidewall angle) are extracted from microscopic images as input to a parameterized geometry model. Optical constants of the involved materials Si and SiO₂ are obtained from tabulated values[33]. A time-harmonic finite-element solver (JCMsuite[34]) is used to construct an

unstructured, prismatoidal mesh of a 2D-periodic unit-cell from the geometry model and to obtain accurate time-harmonic near field solutions of the light scattering problem. Computations are performed for a range of incident plane waves of different incident directions, wavelengths and polarizations. From the near field solution, reflection, transmission, absorption and field energy in specific regions, as well as plots of the field energy distribution are obtained in post-processes on the higher-order finite-element solution. As the computation for a single incident field uses only a small fraction of available computer resources (with computation times of few seconds), parallel execution of the computations on the different CPU cores of one or more workstations is straightforward. Investigating wavelength scans at different numerical resolution levels (by varying the polynomial degree of the finite-element ansatzfunctions) provides information on numerical accuracy of the obtained reflection and field enhancement results. As expected[35], high resolution (low numerical errors, relative errors of the investigated quantities well below 1%) is obtained even with relatively coarse FEM meshes in parameter regions where no optical resonances are excited in the nanohole array. In parameter regions of resonant behavior numerical resolution is increased in order to guarantee low numerical errors.

1. Joannopoulos, J., Johnson, S., Winn, J. & Meade, R. *Photonic Crystals: Molding the Flow of Light (Second Edition)* (Princeton University Press, 2011).
2. Han, S. E. & Chen, G. Optical absorption enhancement in silicon nanohole arrays for solar photovoltaics. *Nano Lett.* **10**, 1012–1015 (2010).
3. Guo, L. J. Nanoimprint lithography: methods and material requirements. *Adv. Mater.* **19**, 495–513 (2007).
4. Battaglia, C. *et al.* Nanoimprint lithography for high-efficiency thin-film silicon solar cells. *Nano Lett.* **11**, 661–665 (2011).
5. Ferry, V. E. *et al.* Optimized Spatial Correlations for Broadband Light Trapping Nanopatterns in High Efficiency Ultrathin Film a-Si:H Solar Cells. *Nano Lett.* **11**, 4239–4245 (2011).
6. Becker, C. *et al.* Polycrystalline silicon thin-film solar cells: Status and perspectives. *Sol. Energ. Mat. Sol. C.* **119**, 112–123 (2013).
7. Belotti, M. *et al.* Replication of photonic crystals by soft ultraviolet-nanoimprint lithography. *J. Appl. Phys.* **99**, 024309 (2006).
8. Zou, Y. *et al.* High-performance, high-index-contrast chalcogenide glass photonics on silicon and unconventional non-planar substrates. *Adv. Opt. Mater.* **2**, 478–486 (2014).
9. Bermel, P., Luo, C., Zeng, L., Kimerling, L. C. & Joannopoulos, J. D. Improving thin-film crystalline silicon solar cell efficiencies with photonic crystals. *Opt. Express* **15**, 16986–17000 (2007).
10. Zeng, L. *et al.* Efficiency enhancement in Si solar cells by textured photonic crystal back reflector. *Appl. Phys. Lett.* **89**, 111111 (2006).
11. Zhou, D. & Biswas, R. Photonic crystal enhanced light-trapping in thin film solar cells. *J. Appl. Phys.* **103**, 093102 (2008).
12. Yu, Z., Raman, A. & Fan, S. Fundamental limit of light trapping in grating structures. *Opt. Express* **18**, A366–A380 (2010).
13. Battaglia, C. *et al.* Light trapping in solar cells: Can periodic beat random? *Nano Lett.* **6**, 2790–2797 (2012).
14. Yablonovitch, E. Statistical ray optics. *J. Opt. Soc. Am.* **72**, 899–907 (1982).
15. Ganesh, N. *et al.* Enhanced fluorescence emission from quantum dots on a photonic crystal surface. *Nat. Nanotechnol.* **2**, 515–520 (2007).
16. Ganesh, N. *et al.* Leaky-mode assisted fluorescence extraction: application to fluorescence enhancement biosensors. *Opt. Express* **16**, 21626–21640 (2008).
17. Fan, X. *et al.* Sensitive optical biosensors for unlabeled targets: A review. *Anal. Chim. Acta* **620**, 8–26 (2008).
18. Lee, M. & Fauchet, P. M. Two-dimensional silicon photonic crystal based biosensing platform for protein detection. *Opt. Express* **15**, 4530–4535 (2007).
19. Tao, C. S., Jiang, J. & Tao, M. Natural resource limitations to terawatt-scale solar cells. *Sol. Energ. Mat. Sol. C.* **95**, 3176–3180 (2011).
20. Senn, T., Bischoff, J., Nüsse, N., Schoengen, M. & Löchel, B. *Photonic. Nanostruct.* **9**, 248–254 (2011).
21. Back, F., Bockmeyer, M., Rudigier-Voigt, E. & Löbmann, P. Hybrid polymer sol–gel material for uv-nanoimprint: microstructure and thermal densification. *J. Sol-Gel Sci. Techol.* **66**, 73–83 (2013).
22. Qin, D., Xia, Y. & Whitesides, G. M. Soft lithography for micro- and nanoscale patterning. *Nat. Protoc.* **5**, 491–502 (2010).
23. Becker, C. *et al.* Direct growth of periodic silicon nanostructures on imprinted glass for photovoltaic and photonic applications. *Phys. Status Solidi C* **9**, 2079–2082 (2012).
24. Merkel, J., Sontheimer, T., Rech, B. & Becker, C. Directional growth and crystallization of silicon thin films prepared by electron-beam evaporation on oblique and textured surfaces. *J. Cryst. Growth* **367**, 126–130 (2013).
25. Haschke, J., Amkreutz, D., Korte, L., Ruske, F. & Rech, B. Towards wafer quality crystalline silicon thin-film solar cells on glass. *Sol. Energ. Mat. Sol. C.* **128**, 190–197 (2014).
26. Tiedje, T., Yablonovitch, E., Cody, G. & Brooks, B. Limiting efficiency of silicon solar cells. *IEEE. T. Electron Dev.* **31**, 711–716 (1984).
27. Yablonovitch, E. & Cody, G. Intensity enhancement in textured optical sheets for solar cells. *IEEE. T. Electron Dev.* **29**, 300–305 (1982).
28. Mallick, S. B., Agrawal, M. & Peumans, P. Optimal light trapping in ultra-thin photonic crystal crystalline silicon solar cells. *Opt. Express* **18**, 5691–5706 (2010).
29. Preidel, V. *et al.* Analysis of absorption enhancement in tailor-made periodic polycrystalline silicon microarrays. *Phys. Status Solidi -R* **7**, 1045–1049 (2013).
30. Schuster, C. S., Bozzola, A., Andreani, L. C. & Krauss, T. F. How to assess light trapping structures versus a lambertian scatterer for solar cells? *Opt. Express* **22**, A542–A551 (2014).
31. Petermann, J. H. *et al.* 19%-efficient and 43 µm-thick crystalline Si solar cell from layer transfer using porous silicon. *Prog. Photovoltaics* **20**, 1–5 (2012).
32. Astratov, V. N. *et al.* Photonic band-structure effects in the reflectivity of periodically patterned waveguides. *Phys. Rev. B* **60**, R16255–R16258 (1999).
33. Palik, E. D. *Handbook of optical constants of solids* (Academic Press, 1985).
34. Pomplun, J., Burger, S., Zschiedrich, L. & Schmidt, F. Adaptive finite element method for simulation of optical nano structures. *Phys. Status Solidi B* **244**, 3419–3434 (2007).
35. Maes, B. *et al.* Simulations of high-Q optical nanocavities with a gradual 1D bandgap. *Opt. Express* **21**, 6794–6806 (2013).

Acknowledgments

Author contributions

C.B. and P.W. conceived and designed the experiments. P.W. performed nanoimprint-lithography and optical measurements. J.P. fabricated the masterstructure via electron-beam lithography. D.E. and V.P. developed the fabrication procedure for silicon nanohole arrays on plastic and glass, respectively. M.H. and S.B. performed optical simulations. C.B. and S.B. wrote the manuscript text. All authors reviewed the manuscript.

Additional information

Competing financial interests: The authors declare no competing financial interests.

How to cite this article: Becker, C. *et al.* 5 × 5 cm² silicon photonic crystal slabs on glass and plastic foil exhibiting broadband absorption and high-intensity near-fields. *Sci. Rep.* **4**, 5886; DOI:10.1038/srep05886 (2014).